Article

Prediction of Heat Transfer in a Jet Cooled Aircraft Engine Compressor Cone Based on Statistical Methods

Fabian Bleier *, Corina Schwitzke and Hans-Jörg Bauer

Karlsruhe Institute of Technology (KIT), Institut für Thermische Strömungsmaschinen (ITS),
76131 Karlsruhe, Germany; corina.schwitzke@kit.edu (C.S.); hans-joerg.bauer@kit.edu (H.-J.B.)
* Correspondence: fabian.bleier@kit.edu; Tel.: +49-721-608-43630

check for updates

Abstract: The paper presents the setup and analysis of an experimental study on heat transfer of a jet cooled compressor rear cone with adjacent conical housing. The main goal of the paper is to describe the systematic derivation of empirical correlations for global Nusselt numbers to be used in the design process of a jet engine secondary air system. Based on the relevant similarity parameters obtained from literature, operating points are deduced leading to a full factorial design experiment to identify all effects and interactions. The varied similarity parameters are the circumferential Reynolds number, the non-dimensional mass flow, the non-dimensional spacing between rotor and stator, and the jet incidence angle. The range of the varied similarity parameters covers engine oriented operating conditions and is therefore suitable to predict Nusselt numbers in the actual engine component. In order to estimate measurement uncertainties, a simplified model of the test specimen, consisting of a convectively cooled flat plate, has been derived. Uncertainties of the measured quantities and derived properties are discussed by means of a linear propagation of uncertainties. A sensitivity study shows the effects of the input parameters and their interactions on the global Nusselt number. Subsequently, an empirical correlation for the global Nusselt numbers is derived using a multivariate non-linear regression. The quality of the empirical correlation is assessed by means of statistical hypotheses and by a comparison between measured and predicted data. The predicted values show excellent agreement with experimental data. In a wide range, accuracies of 15% can be reached when predicting global Nusselt numbers. Furthermore, the results of the sensitivity study show that pre-swirled cooling air does not have a positive effect on heat transfer.

Keywords: jet engines; rotor-stator systems; heat transfer; nusselt number correlation; multivariate regression; statistical modeling

1. Introduction

Increasing the efficiency and decreasing pollutant emissions is the main goal in developing future jet engines. A promising way to reach higher efficiencies is to realise higher engine pressure ratios. While currently pressure ratios of approximately 40 are state of the art, future jet engines will be able to reach pressure ratios of 60 and higher [1]. Among others, this entails rising fluid temperature at the high pressure compressor outlet. In order to guarantee structural and thermal integrity of the compressor rotor, cooling of the compressor becomes necessary. Jet cooling of the compressor rear cone, which can be found between the last stage of the high-pressure compressor and the high-pressure shaft, is a possible concept to decrease the occurring thermal and structural loads and thus to increase lifetime. Cooling air can be taken from the inner diffusor upstream the combustion chamber and the high pressure turbine and led through a heat exchanger (for a possible air cooling concept, see [2]). Afterwards, the cooling air enters the rotor-stator cavity through an array of nozzles and flows radially inwards towards the high pressure shaft. A more detailed description of the cooling assembly is

given in [3,4]. In order to design an efficient cooling system, detailed knowledge on the heat transfer between the rotor-stator cavity and the rotor is necessary. As no literature is available for jet cooling of a rotating cone, a test rig was developed at the Institut für Thermische Strömungsmaschinen (ITS) at Karlsruhe Institute of Technology (KIT) [4] and experiments were conducted, covering a wide range of engine conditions. Furthermore, CFD studies [3] were carried out to identify fundamental effects concerning heat transfer and fluid friction in advance. Main objectives are the reduction of the total relative temperature of the cooling air, and an efficient cooling of the rotor structure with respect to reduced frictional heating and increased heat transfer.

In jet engines, fluid dynamics and heat transfer in cavities between rotating and stationary parts are of huge interest. A comprehensive literature overview of current research on rotor-stator and rotor-rotor cavities is given in [5–7]. However, discoidal rotor-stator systems with or without superposed flow are the most common configurations. Therefore, heat transfer and aerodynamics in discoidal rotor-stator systems have been intensively investigated in the past. A detailed summary of the theory and a detailed literature survey was published by Owen and Rogers [8].

Conical rotor-stator systems were hardly investigated in the past. To the authors' knowledge, a single experimental heat transfer study of Alexiou et al. [9] exists, where Nusselt numbers on a jet engine compressor rear cone without adjacent casing were determined. However, aerodynamic studies on enclosed cylinders, cones, and discs with constant gap width were performed by Wimmer and Zierep [10]. For sufficiently high rotational velocities and cone angles, results for the conical rotor-stator configuration show a flow regime similar to that found in the discoidal one. A detailed numerical and experimental study of the flow field in a compressor rear cone at large relative spacing is presented in [11]. For no superposed flow the authors find a similar flow structure of the conical rotor-stator system and a discoidal one. With regard to the present case with high rotational velocities and a medium cone angle of $\theta \approx 35°$, the aerodynamic and heat transfer are expected to be similar to those of a discoidal rotor-stator system.

Heat transfer results for a discoidal rotor-stator system without superposed flow were first published by Dorfman [12]. In accordance with the torque measurements of Daily and Nece [13], four heat transfer regimes were found depending on the circumferential Reynolds number Re_φ and the relative spacing G between rotor and stator. In Figure 1 the heat transfer results from Pellé and Harmand [14] for an open discoidal rotor-stator system without a superposed flow of air are depicted. For low circumferential Reynolds numbers and a low relative spacing between rotor and stator, laminar flow with merged rotor and stator boundary layer occurs. Based on the aerodynamic results of Owen and Rogers [8], Daily and Nece [13], surface averaged Nusselt numbers can be derived [14] yielding

$$\overline{Nu} = G^{-1} \tag{1}$$

for regime I. With increasing spacing between rotor and stator the boundary layers separate and an inviscid core between the rotor and stator boundary layer exists (regime II). Nusselt numbers can be correlated by

$$\overline{Nu} = 0.5940 \cdot G^{1/10} \cdot Re_\varphi^{1/2} \tag{2}$$

for regime II. For low relative spacing and increasing circumferential Reynolds numbers, a transition from laminar to turbulent flow (regime III) occurs. In this region, the global Nusselt number

$$\overline{Nu} = 0.009\,804 \cdot G^{-1/4} \cdot Re_\varphi^{3/4} \tag{3}$$

increases with decreasing relative spacing G and with increasing circumferential Reynolds number Re_φ. Another transition to regime IV can be observed for turbulent flow with increasing relative spacing. Similar to regime II, boundary layers are separated at high relative spacing leading to the Nusselt number correlation

$$\overline{Nu} = 0.0162 \cdot G^{1/10} \cdot Re_\varphi^{4/5}. \tag{4}$$

Due to the high circumferential Reynolds number and the low relative spacing, regimes III and IV are likely to occur in the presented rotor-stator system.
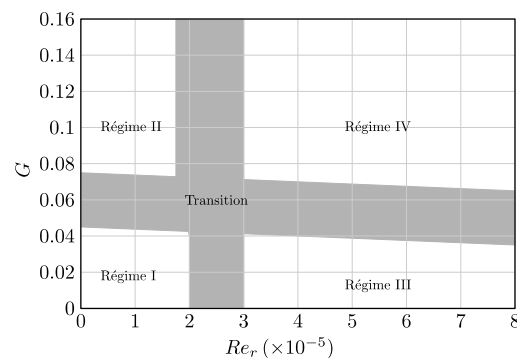
Figure 1. Heat transfer regimes for an open discoidal rotor-stator system (Reprinted from [14] with permission from Elsevier): regime I (laminar, merged boundary layers), regime II (laminar, separated boundary layers), regime III (turbulent, merged boundary layers), and regime IV (turbulent, separated boundary layers).

For the present case of a rotor-stator system with a superposed radial inflow, only a few heat transfer studies are available. Those in a radial turbine of Mitchell and Metzger [15] show a dependency of the global Nusselt number $\overline{Nu}$ on the mass flow C_w, the spacing G, and the circumferential Reynolds number Re_φ. Recent experimental results by Djaoui et al. [16] reveal a large effect of the inflow conditions on the stator Nusselt number of a discoidal rotor-stator system with superposed inflow.

Planning experiments and analysing data [17] by using statistical methods are sparsely found in literature, as most authors compare their results to well-documented basic experiments and correlations. To get a first overview of the data and to identify the most important input parameters and interactions, statistical methods provide many ways to thoroughly characterize a physical problem. Therefore, the main goal of the present work is to derive empirical correlations to obtain global Nusselt numbers for a jet cooled conical rotor-stator cavity. The work especially focuses on the setup of the experiments using systematic statistical approaches. Fundamental physical effects will be discussed based on a sensitivity study.

In the first section of this work, the experimental procedure, the governing similarity parameters, and the parameter space are described. The subsequent section contains the discussion of the measurement uncertainty, and the influence of the predefined similarity parameters is discussed by means of a sensitivity study. Based on the observed effects and interactions, the actual derivation of correlations by using a multivariate regression is done. Finally, the suitable quality of the correlation is verified by a comparison between measured and predicted data.

2. Experimental Procedure

A brief description of the physical problem and the test rig setup will be given below; for further information on the test rig, refer to [4] and to Appendix A. The test rig setup is based on the generic rotor-stator system depicted in Figure 2. Jet cooling is realized by an array of 48 nozzles with incidence angle γ in order to achieve variable inflow conditions. In contrast to the real application and due to design restrictions, the rotor structure is heated by the incoming jet [3]. After entering the rotor-stator cavity, impinging the rotor surface at radius r_1 air flows radially inwards, while a small amount of leakage air $\dot{m}_L$ flows radially outwards. The main air flow supplies heat to the rotor and leaves the cavity at radius r_i. The locally supplied heat can be expressed by means of the local Nusselt number

$$Nu\left(r\right) = \frac{r_o}{k_f} \cdot h\left(r\right) = \frac{r_o}{k_f} \cdot \frac{\dot{q}_S\left(r\right)}{T_{W,ad}\left(r\right) - T_{W,h}\left(r\right)} \tag{5}$$

depending on the characteristic length scale r_o, the fluid thermal conductivity k_f, the surface heat flux density $\dot{q}_S$, and the adiabatic wall temperature difference $T_{W,ad} - T_{W,h}$, where $T_{W,ad}$ is the adiabatic wall temperature (see Appendix B). With respect to the dimensioning of a secondary air system, the total amount of heat $\dot{Q}_S$ transferred between the inlet at r_1 and the outlet of the rotor-stator system at r_i is of main interest. Therefore, the global (or surface averaged) Nusselt number is defined [8] according to

$$\overline{Nu}\,(r^*) = \frac{r_o}{k_f} \cdot \frac{\dot{Q}_S/A}{T_{W,ad} - T_{W,h}} = \frac{r_o}{k_f} \cdot \frac{\int_{r_1}^{r^*} \dot{q}_S \, \mathrm{d}A}{\int_{r_1}^{r^*} (T_{W,ad} - T_{W,h}) \, \mathrm{d}A} = \frac{\int_{r_1}^{r^*} Nu \cdot (T_{W,ad} - T_{W,h}) \, \mathrm{d}A}{\int_{r_1}^{r^*} (T_{W,ad} - T_{W,h}) \, \mathrm{d}A}, \quad (6)$$

where Equation (5) has been applied and the differential conical surface $\mathrm{d}A = 2\pi r \mathrm{d}r / \sin\theta$.

Figure 2. Scheme of the physical problem with variable input parameters and test rig setup with schematic illustration of the temperature measurements (■) [4].

The main challenge of the experimental procedure is therefore to estimate the surface heat flux density $\dot{q}_S$ based on the rotor surface temperatures of the inner and outer rotor surface (Figure 2, red squares). The temperature measurements are done by means of 28 K-type thermocouples from which 12 are located at the inner rotor surface and 16 at the outer rotor surface. Signal transmission between the rotating temperature sensors and the evaluation unit is done by a 28-channel telemetry unit. Measured temperatures are interpolated and set as boundary conditions of a two-dimensional, axisymmetric finite-element model of the rotor. Solving the heat equation for the rotor structure provides the surface heat flux density $\dot{q}_S$ (see Appendix A). The results of the finite-element analysis are finally inserted into Equation (6) to calculate global Nusselt numbers.

The objective of the experimental work is to derive an empirical correlation for determining the global Nusselt number $\overline{Nu}$ between the inlet of the rotor-stator system and the evaluation radius $r^* \approx 0.5 \cdot r_o$ at the most inner measurement position next to the outlet radius r_i, depicted in Figure 2. The evaluation radius r^* has been chosen in order to avoid extrapolation of the measured data to the inner radius r_i. The evaluation is based on the design parameters derived in the literature survey and is expected to have a significant effect on the global Nusselt number and is therefore discussed in the following section.

2.1. Design Parameters

According to the heat transfer results of Mitchell and Metzger [15], the rotational velocity, the superposed mass flow, and the gap width have a major effect on the heat transfer in a rotor-stator gap with a radial inflow. Furthermore, the results of Pellé and Harmand [14] reveal a large effect of the inflow conditions. The inflow conditions mainly depend on the tangential velocity component

of the gap inlet velocity which is a function of the incidence angle γ and the superposed mass flow. These properties are varied within the experimental study. Besides the variable parameters, there are several constant or dependent non-dimensional groups, denoted as non-variable parameters.

The design parameters varied during the test campaign are defined based on the design of a pre-swirl system of a rotor-stator assembly in a jet engine. For different engines, several non-dimensional gap widths G between rotor and adjacent stator can be found. During operation, the rotational Reynolds number Re_φ and the cooling air mass flow rate C_w might change. In addition, the inflow conditions are mainly determined by the jet incidence angle γ and can be varied from no pre-swirl ($\gamma = 90°$) to maximum pre-swirl ($\gamma = 30°$). A schematic of the experimental study and the variable and non-variable parameters is illustrated in Figure 3. The definitions of the non-dimensional groups and the parameter range realized in the study can be found in Table 1. For guidance, typical parameter ranges of jet engines are added. The data ranges are taken from literature [8,9,18] or are derived from authors' calculations.
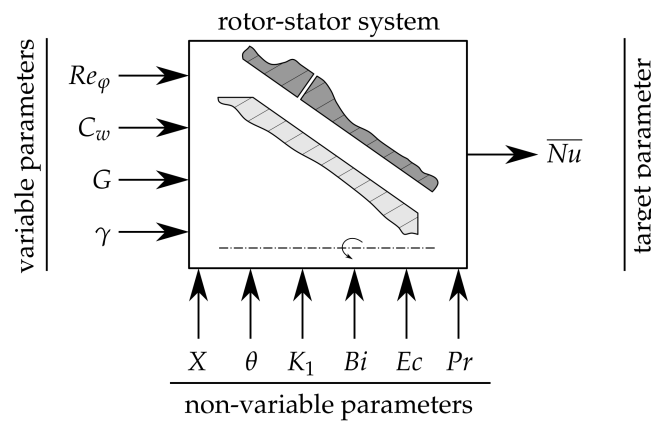
Figure 3. Geometric and thermodynamic parameters influencing the target parameter.

Table 1. Variable and non-variable parameters and corresponding value ranges.

Parameter	Definition	Test Rig Conditions	Engine Conditions [8,9,18]
Circ. Reynolds number Re_φ	$\left(\omega \cdot r_o^2 \cdot \varrho\right)/\mu$	$<5 \cdot 10^6$	$>10 \cdot 10^6$
Non-dim. mass flow rate C_w	$\dot{m}/\left(\mu \cdot r_o\right)$	$16 \cdot 10^3$ to $25 \cdot 10^3$	$5 \cdot 10^3$ to $50 \cdot 10^3$
Relative gap width G	s/r_o	0.03 to 0.11	>0.05
Incidence angle γ		$\frac{\pi}{6}$ to $\frac{\pi}{2}$	$\frac{\pi}{6}$ to $\frac{\pi}{2}$
Jet diameter ratio D	$d/\left(2 \cdot r_o\right)$	$6.82 \cdot 10^{-3}$	tbd
Number of jets n		48	tbd
Leakage mass flow rate C_{wL}	$\dot{m}_L/\left(\mu \cdot r_o\right)$	$8 \cdot 10^3$	
Diameter ratio X	r_i/r_o	0.45	>0.4
Cone angle θ		$35°$	$36°$
Initial swirl ratio K_1	$u_{\varphi,\text{jet}}/\left(\omega \cdot r_o\right)$	<1.4	<1.5
Biot number Bi	$h \cdot H/k_S$	0.2 to 5	0.1 to 5
Eckert number Ec	$\Delta u_\varphi^2/\left(c_p \cdot \Delta T\right)$	<2	<1
Prandtl number Pr	$c_p \cdot \mu/k_f$	0.71	0.72

2.2. Design Parameter Space

With respect to the scope of this work, which is to identify the influence of similarity parameters on the global Nusselt number, some preliminary considerations have to be made in order to define a suitable test plan. Determining if there is a linear correlation or no correlation between input and target parameters requires at least two factor levels of each input parameter. Accordingly, higher order non-linear correlations require three or more factor levels of input parameters. Thus, to identify the

effects of all the four variable parameters Re_φ, C_w, G, and γ and their interactions, at least $3^4 = 81$ single experiments are required, which matches a full factorial design experiment.
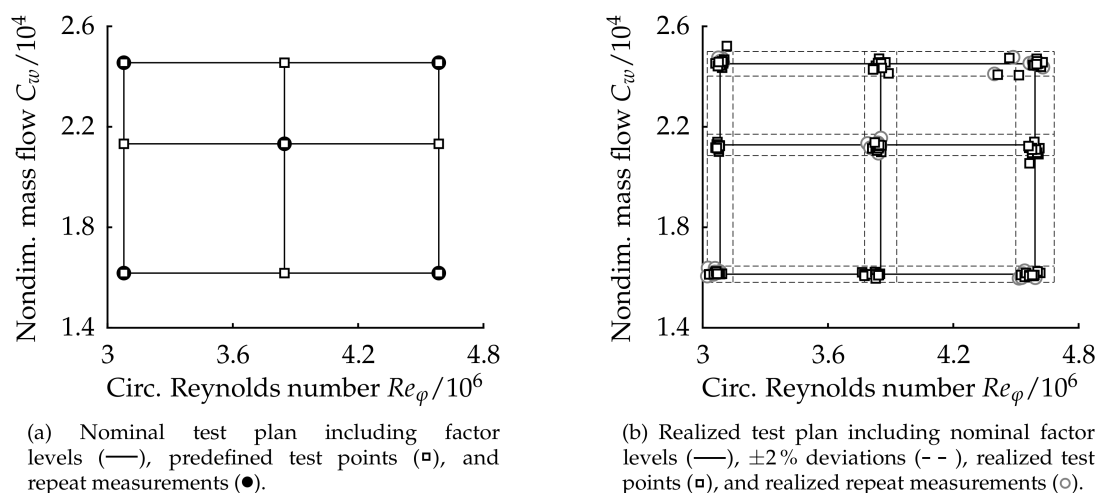
In order to efficiently discuss effects and interactions, all variable parameters were divided into discrete groups whose nominal values or factor levels refer to numbers from 1 to 3 or 4. The assignment between groups and factor levels can be taken from Table 2. The range of parameters is limited by the test rig capabilities as presented in Table 1. The operating conditions were chosen taking into account test rig limitations (e.g., vibrations), and reaching an optimum measurement accuracy.

Table 2. Grouped variable parameters and their nominal values or factor levels.

Group	$Re_\varphi/10^6$	$C_w/10^4$	G	γ
1	3.08	1.61	0.03	$\pi/6$
2	3.83	2.12	0.07	$\pi/4$
3	4.57	2.45	0.11	$\pi/3$
4	–	–	–	$\pi/2$

The chart in Figure 4a shows the resulting test points dependent on the circumferential Reynolds number Re_φ and the mass flow rate C_w, which will be repeated for all geometric variations of G and γ as listed in Table 2. The test points for the repeat measurements were chosen based on a Box-Behnken design, where the extreme points and the centre point of the experiment include repeat measurements, denoted by the filled circles in Figure 4a. Consequently, 14 single experiments including 5 repeated points were performed for each of 12 different geometries, leading to a total of 108 samples to be used to derive a correlation. The experimentally reached test points are illustrated in Figure 4b. The solid lines represent the factor levels of the nominal values while the dashed lines are $\pm2\%$ deviations. Most test points lie within the $\pm2\%$ interval. The test points slightly outside the interval result from the fact that the nominal test points were located next to natural frequencies of the test rig and therefore had to be shifted to lower rotational velocities.

The following discussion of the results and the derivation of a correlation is based on the discrete groups introduced in Table 2.

(a) Nominal test plan including factor levels (——), predefined test points (▫), and repeat measurements (●).

(b) Realized test plan including nominal factor levels (——), $\pm2\%$ deviations (- -), realized test points (▫), and realized repeat measurements (○).

Figure 4. Comparison between nominal test plan and realized test plan for Reynolds number Re_φ and mass flow C_w.

3. Results and Discussion

With regard to a critical discussion of the results, the first step is an uncertainty analysis of the complete measuring chain. The uncertainty analysis is followed by a sensitivity study to find the main

effects and interactions influencing the global Nusselt number. Finally, the correlation to predict a global Nusselt number is derived and discussed.

3.1. Measurement Uncertainty

Due to the complexity of the two-dimensional heat transfer problem, a simplified model according to Figure 5 has been defined in order to calculate a linear propagation of uncertainties. The model consists of a cylinder with a sufficiently large radius r, a uniform surface temperature distribution at the inner and outer surface and a constant heat flux density across the structure. For this one-dimensional configuration, Equation (6) simplifies to

$$\overline{Nu} = \frac{L}{k_f} \cdot \frac{\dot{q}_S}{T_{f,h} - T_{W,h}} = \frac{L}{H} \cdot \frac{k_S}{k_f} \cdot \left(\frac{T_{W,h} - T_{W,c}}{T_{f,h} - T_{W,h}} \right) = \frac{L}{H} \cdot \frac{k_S}{k_f} \cdot \frac{\Delta T_W}{\Delta T_f}, \tag{7}$$

where L is the characteristic length scale, and $T_{f,c}$ and $T_{f,h}$ are the total temperatures of the flow on the hot and the cold side, respectively. Consequently, the resulting uncertainty depends on the relative uncertainty of the wall thickness measurement H, of the characteristic length L, the thermal conductivities k_S and k_f, and the differential temperature measurements ΔT_W and ΔT_f. While the relative measurement uncertainty for the thickness and the thermal conductivity is assumed to be constant, the relative uncertainty of temperature changes with the temperature differences leading to a maximum uncertainty of global Nusselt numbers

$$\frac{\Delta \overline{Nu}}{\overline{Nu}} = \frac{\Delta k_S}{k_S} + \frac{\Delta k_f}{k_f} + \frac{\Delta L}{L} + \frac{\Delta H}{H} + \frac{\Delta (\Delta T_W)}{\Delta T_W} + \frac{\Delta (\Delta T_f)}{\Delta T_f}. \tag{8}$$

The $\Delta (\dots)$ values represent the absolute measurement uncertainties. The wall temperature difference ΔT_W and the hot air temperature difference ΔT_f are dependent on the heat transfer, and thus the Nusselt number uncertainty $\Delta \overline{Nu}/\overline{Nu}$ is a function of the heat transfer, too.
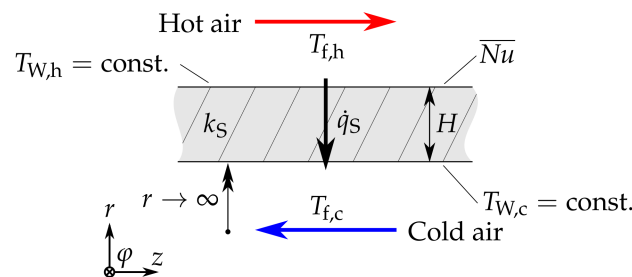
Figure 5. Comparison between nominal test plan and realized test plan for Reynolds number Re_φ and mass flow C_w.

An uncertainty estimation based on the one-dimensional heat transfer problem results in a distribution of maximum relative uncertainties according to Figure 6a. The plot shows that uncertainties less than approximately 12% can be reached for most test points. As mentioned in Section 2, several operating points were repeated to confirm the proper setup and repeatability of the experiment. The deviation between the repeated and nominal test points is plotted in Figure 6b indicating a standard deviation for the temperature measurements of 2.5% or less for most test points. With regard to the standard deviations of the operating points of approximately $\pm 2\%$, Figure 6b indicates an excellent repeatability of the experiments.
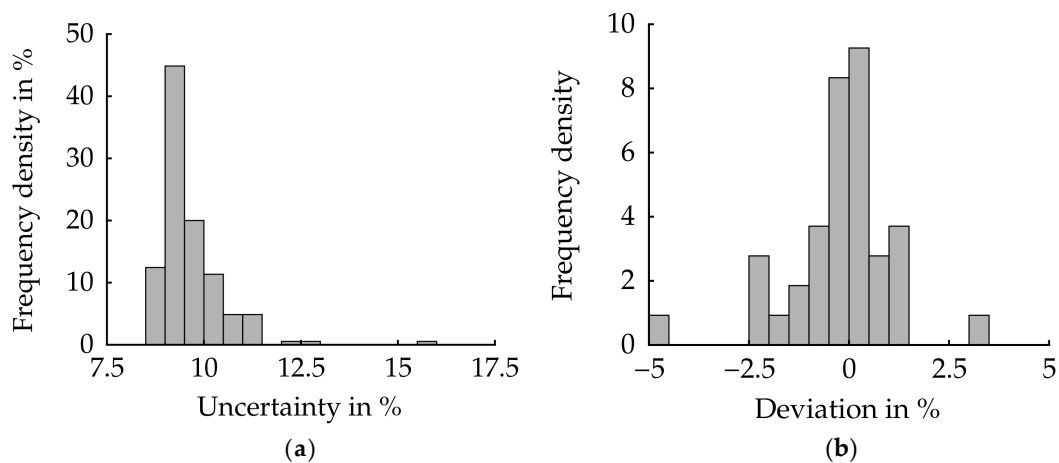
Figure 6. Detailed uncertainty analysis including linear propagation of uncertainties and repeatability of the experiments. (**a**) Nusselt number uncertainty for all measurements. (**b**) Deviation between repeated measurements.

3.2. Sensitivity Study

The aim of the following sensitivity study is to identify the correlations between the global Nusselt number and the variable parameters Re_φ, C_w, G, γ. Furthermore, possible interactions between the input parameters must be identified in order to derive an empirical correlation suitable for determining global Nusselt numbers.

The chart depicted in Figure 7 contains the sample averaged relative changes of the global Nusselt numbers $\overline{\overline{\Delta Nu}}$, when a single parameter is changed from the lowest (1) to the highest factor level (3 or 4) (see Table 2). For example, the relative effect of the circumferential Reynolds number is calculated such that

$$\overline{\delta Nu}\left(Re_\varphi\right) = \frac{\overline{\overline{Nu}}\left(C_{wi}, G_j, \gamma_k, Re_{\varphi 3}\right)}{\overline{\overline{Nu}}\left(C_{wi}, G_j, \gamma_k, Re_{\varphi 1}\right)} - 1, \tag{9}$$

where i, j, k are the factor levels of the variable parameters according to Table 2. It can be seen that increasing the circumferential Reynolds number Re_φ or increasing the incidence angle γ both result in a large increase of the averaged Nusselt number of 43% and 67%, respectively. Consequently, an empirical correlation must take into account the positive correlation between these two parameters and the global Nusselt number. The increase of the non-dimensional gap width G in turn leads to a large decrease of the global Nusselt number of -31%. No significant effect of the mass flow C_w on the global Nusselt number can be found and the corresponding change of the relative global Nusselt number is approximately 0. The observed main effects confirm the results derived from previous studies (see Section 1). In rotor-stator systems, the circumferential Reynolds number Re_φ and the relative spacing G are the dominant parameters to describe the heat transfer. The negative effect of the relative spacing indicates that the present rotor-stator flow is similar to regime III, and further studies are necessary to prove this observation. The most important effect in the present case comes from the incidence angle γ which defines the tangential velocity component of the inlet air.
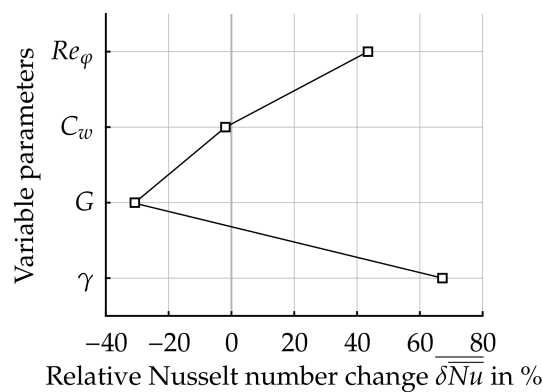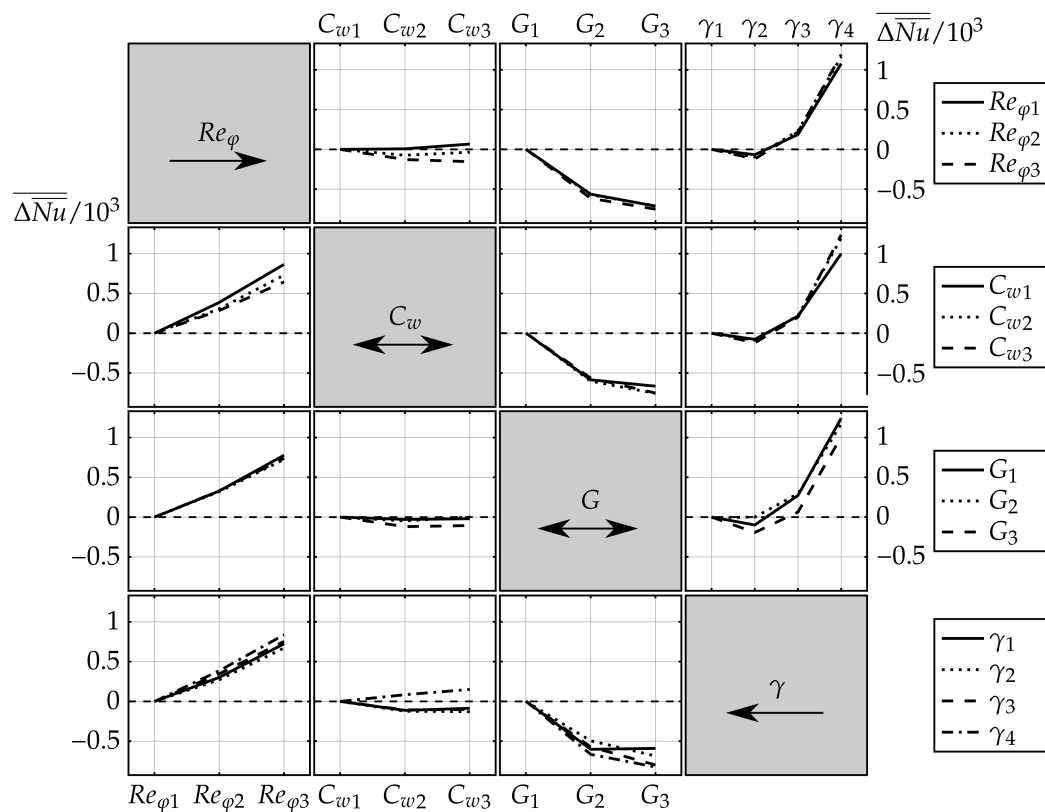
Figure 7. Main effects of all variable parameters on the averaged relative Nusselt number change $\overline{\overline{\delta Nu}}$.

However, the above figure does not contain any information about possible interactions between the variable parameters. To identify these interactions, Figure 8 shows the charts for all 12 combinations between the variable parameters. One single chart illustrates the average change of the Nusselt number caused by the variation of a single parameter for the factor levels of another parameter, drawn as an array of curves. The definition of the averaged Nusselt number change for the combined change of variable parameters is similar to Equation (9). Data points illustrating an interaction between the circumferential Reynolds number $Re_{\varphi i}$ and the mass flow rate C_{wj} (Row 2, Column 1) are calculated according to

$$\overline{\Delta Nu}\left(Re_{\varphi i}, C_{wj}\right) = \overline{Nu}\left(Re_{\varphi i}, C_{wj}, G_k, \gamma_l\right) - \overline{Nu}\left(Re_{\varphi 1}, C_{wj}, G_k, \gamma_l\right). \tag{10}$$

To find all interactions, the indices i, j, k, l are permuted according to the factor levels of the variable parameters in Table 2. Thus, the chart in Row 2 and Column 1 indicates the effect of the circumferential Reynolds number Re_φ with changing mass flow rate C_w with reference to the cases where $i = 1$. If all curves coincide, no interaction between the corresponding variable parameters can be found (e.g., in case of the first row, an interaction between the circumferential Reynolds number Re_φ and the mass flow C_w can be found in the second column). The corresponding chart (Row 1, Column 2) indicates that the slope of the curves for different Reynolds numbers changes with changing mass flow.

Accordingly, the same interaction can be found vice versa (Row 2, Column 1), indicating a decreasing effect of the circumferential Reynolds number on the global Nusselt number with increasing mass flow. The observed interaction can be explained by the relative velocity between the rotor surface and the surrounding air, which changes for a constant circumferential Reynolds number Re_φ and increasing mass flow C_w and therefore affects the local heat transfer. Another significant interaction can be observed between the mass flow C_w and the incidence angle γ. The corresponding charts (R2, C4; R4, C2) indicate an increasing slope of the $\overline{Nu}$–γ dependency for increasing mass flows. On the other hand, increasing incidence angles result in an increasing slope of the effect of the mass flow C_w on the global Nusselt number $\overline{Nu}$. The observation shows that the inflow conditions which depend on the mass flow and the incidence angle strongly affect the heat transfer in a rotor-stator system with radial inflow. This fact has already been found in previous studies [14]. Between the geometric parameters G and γ, a third interaction can be identified based on Figure 8 (C3, R4; C4, R3), leading to an increasing effect of the incidence angle γ with decreasing gap width G.

Figure 8. Illustration of the interactions between the variable parameters and their effect on the averaged global Nusselt number $\overline{\overline{\Delta Nu}}$.

Results show that the main effect on the global Nusselt number is caused by the jet incidence angle γ. By choosing an appropriate value for the incidence angle, the global Nusselt number can be varied about 1000. Taking into account the effect of the gap width G, Nusselt number changes of more than 200% can be realized. With regard to a maximum heat transfer, the smallest gap width $G_1 \approx 0.03$, and the largest incidence angle $\gamma_4 = 90°$ yield an optimum configuration.

A summary of the main effects and interactions is given in Table 3. The major diagonal of the matrix represents the main effects of the corresponding parameters, which are dominant compared to the interactions, represented by the minor diagonals. Plus signs indicate a positive (increasing), minus signs a negative (decreasing) effect. For interactions, a plus sign means an increasing effect of one parameter if the other parameter increases. The minus sign indicates a decreasing effect of one parameter when increasing the other parameter. If no effect or interaction was observed, a ○ is inserted. Based on these observations and the summary from Table 3, the general form of the empirical correlation can be derived. In a second step, remaining coefficients and exponents will be fitted, which is the objective of the following section.

Table 3. Summary of the observed main effects (major diagonal) and interactions (minor diagonals) for increasing the variable parameters from the lowest to the highest factor level.

	Re_φ	C_w	G	γ
Re_φ	$++$	$-$	○	○
C_w	$-$	○	○	$+$
G	○	○	$--$	$+$
γ	○	$+$	$+$	$+++$

3.3. Derived Correlation

Within the last section of the present study, an empirical correlation will be derived including the observations obtained from the sensitivity study. Using a common products of powers approach [8,14], including all effects and interactions leads to the generic correlation for the predicted Nusselt number

$$\overline{Nu}^* = C \cdot \underbrace{\prod_{i=1}^{4} P_i^{e_i}}_{\text{Main effects}} \cdot \underbrace{\prod_{i,j=1}^{4} P_i^{e_{i,j}P_j}}_{\text{Interactions}}, \ i \neq j, \tag{11}$$

where P_i and P_j are the variable parameters, C is a coefficient, and $e_{i,j}$ are exponents. The results summarized in Table 3 indicate three main effects (Re_φ, G, γ) and three interactions ($Re_\varphi - C_w$, $\gamma - C_w$, $\gamma - G$). Therefore, six exponents and one constant from the generic correlation from Equation (11) must be estimated, as all other effects and interactions are negligible. A nonlinear, multivariate regression based on a least-squares fit [19] is used to estimate the coefficient C and the exponents $e_{i,j}$. In order to derive the correlation, no repeated data was used for the fit. The robustness of the generic correlation has been proven by randomly deleting up to 50 data points of the least-squares fit, leading to a variation of the estimated constant and exponents in the order of only 1%. The approach gives the correlation
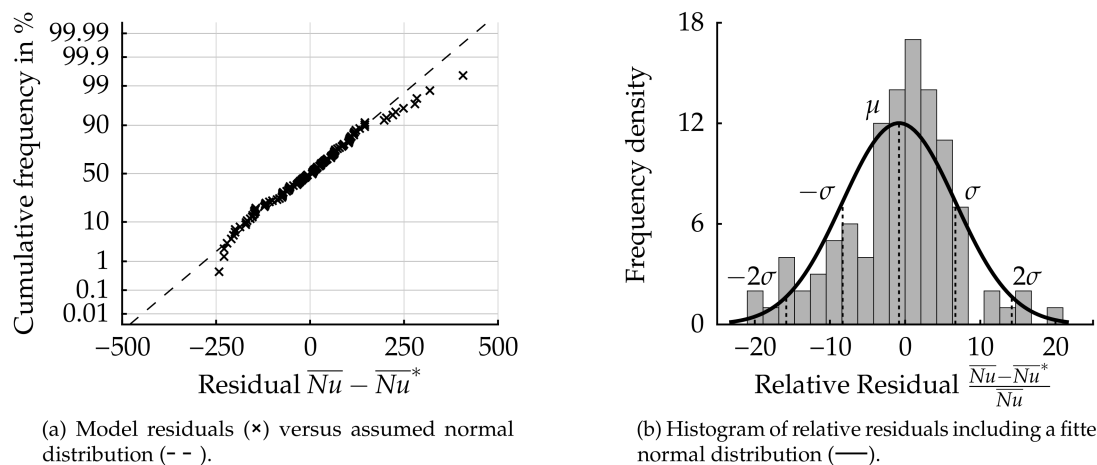
$$\overline{Nu}^* = 281.98 \cdot \underbrace{\frac{(Re_\varphi/10^6)^{0.8}}{\cos \gamma^{0.005} \cdot G^{0.3}}}_{\text{Main effects}} \cdot \underbrace{\frac{(Re_\varphi/10^6)^{4 \cdot 10^{-6}C_w}}{\cos \gamma^{0.04G} \cdot (C_w/10^4)^{0.4\cos\gamma}}}_{\text{Interactions}}, \tag{12}$$

where the incidence angle γ has been transformed with the cosine function to account for the nonlinear shape of the curves depicted in Figure 8. The first factor of Equation (12) includes all main effects observed in Section 3.2. Moreover, all observed interactions are taken into account in the second factor of the correlation. Therefore, the correlation is expected to allow for Nusselt number predictions within the parameter ranges $3 \cdot 10^6 < Re_\varphi < 4.6 \cdot 10^6$, $1.6 \cdot 10^4 < C_w < 2.4 \cdot 10^4$, $0.03 < G < 0.11$, and $30° < \gamma < 90°$ with high accuracy. It is notable that the estimated exponent of the relative spacing G is similar to the one found for regime III (Equation (3)) of rotor-stator systems without a superposed flow. For the circumferential Reynolds number Re_φ the exponent is identical to the one found for regime IV (Equation (4)). As the realised spacing of the present study covers the transition regions between those two regimes (see, Figure 1), further investigations are necessary to completely understand the aerodynamics and heat transfer of rotor-stator systems with superposed centripetal flow. The quality of the derived correlation will be assessed in the following section.

3.4. Correlation Quality

Assessing the quality of the derived correlation follows according to Figure 9. The chart in Figure 9a shows the distribution of the absolute residuals between the measured data and the predicted data. The dashed line represents the frequencies for a normal distribution of the residuals. Residuals which coincide with the normal distribution can be interpreted as stochastic deviations between predicted and measured data.

It can be concluded that most of the residuals can be described as stochastic deviations. For only 1% of the negative residuals, and 10% of the positive residuals, coincidence with the virtual normal distribution is worse. The corresponding residuals are likely caused by systematic model errors leading to the deviations between the empirical correlation and the measured data. Possible reasons for model errors could be missing interactions of three or more variable parameters, which were not considered within the present study.

(a) Model residuals (×) versus assumed normal distribution (- -).

(b) Histogram of relative residuals including a fitted normal distribution (—).

Figure 9. Absolute and relative distribution of the residuals between predicted Nusselt numbers $\overline{Nu}^*$ and measured global Nusselt numbers $\overline{Nu}$.

In Figure 9b, the frequency density function of the relative residuals is depicted. Additionally, a normal distribution is added in order to derive an approximate standard deviation of the empirical correlation. The maximum relative error between prediction and measurement has a value of $\pm 20\%$, whereas more than 95% of the relative errors are less than approximately 15.1%, indicating an excellent accuracy of the derived correlation.

The quality of the derived correlation and of the predicted global Nusselt numbers can be assessed by the set of parameters presented in Table 4.

Table 4. Quality parameters of the correlation according to (Equation (12)).

R^2 in %	RMSE	μ in %	σ in %
96.3	129	−0.812	7.53

The resulting coefficient of determination R^2 reaches a value of 96.3%, indicating a good adaption between model function and measured data as well as the root mean square error (RMSE) of 129. The deviations between predicted and measured data according to Figure 9b can approximately be described by an almost symmetric normal distribution with a standard deviation of $\sigma \approx 7.53\%$. As already mentioned, the maximum error of the correlation is expected to be within 20% for the parameter range discussed above. Therefore, the empirical correlation is judged to be suitable to predict global Nusselt numbers for the parameter range according to Table 1.

A comparison between the measured global Nusselt numbers (symbols) and the derived correlation (lines) can be found in Figure 10. The figures depict the global Nusselt number as a function of the mass flow rate C_w for the tested circumferential Reynolds numbers Re_φ (lines and symbols), and the relative spacing G (colors). In Figure 10a the results for the incidence angle $\gamma_1 = 30°$ are depicted. While the calculated and measured Nusselt numbers are generally in good agreement, larger deviations can be found for $Re_{\varphi 1}$, G_1 (–○–). In this case, the correlation shows a decreasing Nusselt number with increasing mass flow rate, while the experimental results indicate an increasing Nusselt number. The same trend can be observed for $Re_{\varphi 1}$, and the relative spacing G_2 (–○–). For the case $Re_{\varphi 3}$ and G_3 (··◇··) larger deviations of 20 % can be found, whereas the qualitative dependency is predicted correctly. The comparison for the incidence angle $\gamma_2 = 45°$ according to Figure 10b shows a similar effect, but the correlation generally over predicts the Nusselt numbers and underestimates the influence of the mass flow rate C_w for higher gap widths G_2 and G_3. This trend can also be observed for the incidence angle $\gamma_3 = 60°$ depicted in Figure 10c, while the quantitative deviations

between measured and predicted data is small. In case of the largest incidence angle $\gamma_4 = 90°$ both the qualitative and the quantitative agreement between predicted and measured data is excellent.

(a) Incidence angle $\gamma_1 = 30°$.

(b) Incidence angle $\gamma_2 = 45°$.

(c) Incidence angle $\gamma_3 = 60°$.

(d) Incidence angle $\gamma_4 = 90°$.
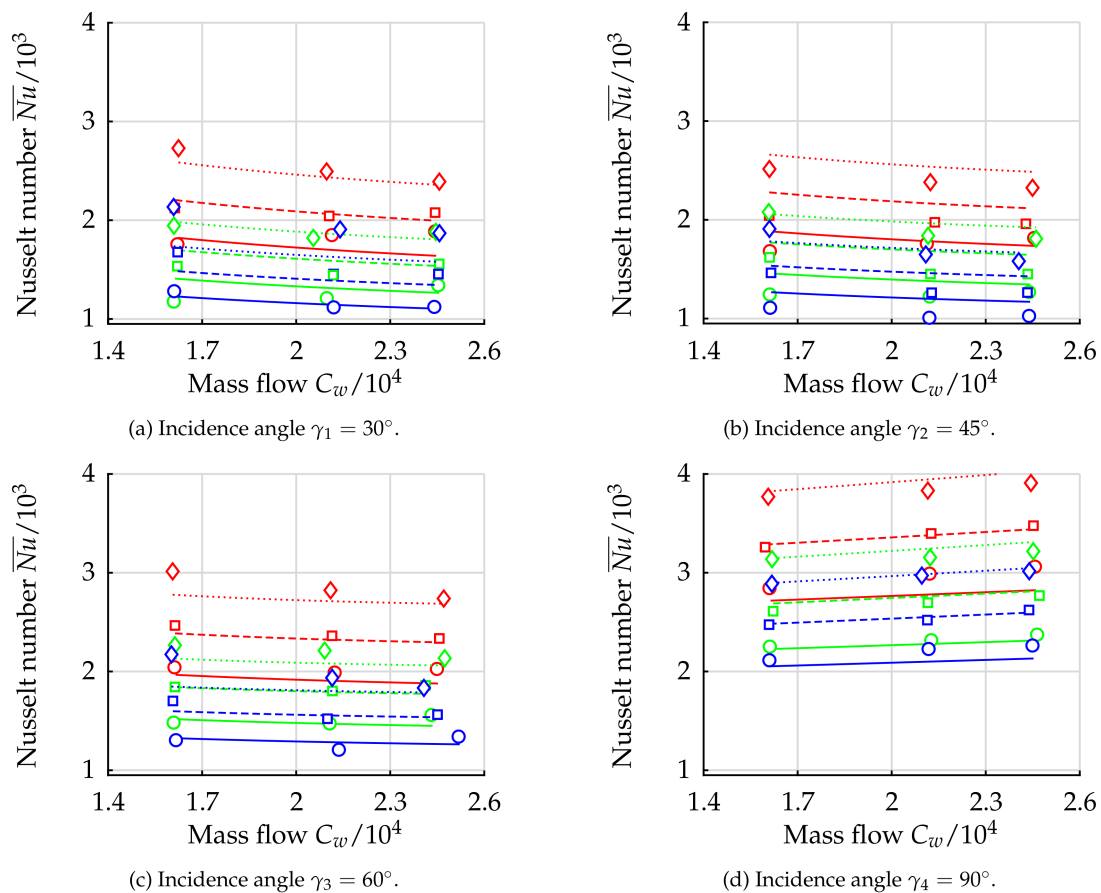
Figure 10. Comparison between measured data (symbols) and the derived correlation (lines) as a function of the mass flow rate C_w for each incidence angle γ and the varations: $Re_{\varphi 1}$: G_1 (—○—), G_2 (—○—), G_3 (—○—); $Re_{\varphi 2}$: G_1 (-□-), G_2 (-□-), G_3 (-□-); $Re_{\varphi 3}$: G_1 (·◇·), G_2 (·◇·), G_3 (·◇·).

4. Summary and Conclusions

The present study presents the setup and analysis of an experiment to derive empirical correlations for global Nusselt numbers of a jet cooled conical rotor-stator system. One objective of the study is the identification of the most important variable parameters which determine the heat transfer. Therefore, the governing similarity parameters of the problem were introduced from previous publications. Consequently, the circumferential Reynolds number Re_{φ}, the dimensionless mass flow rate C_w, the relative rotor-stator spacing G, and the incidence angle γ of the jet cooling were chosen as variable parameters for the experiments. The experimental setup was based on design of experiments leading to a full factorial test plan in order to identify and separate all main effects and interactions of the variable parameters on the global Nusselt number. The preliminary defined test points could be reached within an uncertainty of ±2% as well as a measurement uncertainty of approximately 10% for most test points.

The most significant physical effects were discussed, based on a sensitivity study. It has been shown that the incidence angle γ of the jet cooling has a major effect on the global Nusselt number, while no significant effect could be observed for the mass flow rate C_w. For the circumferential Reynolds number Re_{φ}, a large positive effect on heat transfer was found, whereas the gap width G has a large negative effect on heat transfer. A maximum heat transfer inside the rotor-stator cavity can be

reached by realizing an incidence angle of the jet cooling $\gamma = 90°$ (no pre-swirl), and a non-dimensional gap width $G \approx 0.03$ for all operation conditions. Furthermore, the results showed that changing the geometry enables a global Nusselt number change of more than 200%, leading to a large variety of different rotor-stator configurations with a tailored heat transfer characteristic.

Finally, an empirical correlation to predict global Nusselt numbers covering the parameter ranges $3 \cdot 10^6 < Re_\varphi < 4.6 \cdot 10^6$, $1.6 \cdot 10^4 < C_w < 2.4 \cdot 10^4$, $0.03 < G < 0.11$, and $30° < \gamma < 90°$ was derived. The quality of the correlation was proven against experimental data, which showed that the empirical correlation includes the most significant effects and interactions. With the largest deviations between measured and predicted data of 15% for 95% of the measured data, the correlation is suitable to predict heat transfer in a conical rotor-stator cavity for the given range of variable parameters. Based on the correlation, the geometry of the compressor rear cone can be optimized to meet specific requirements of heat transfer in the rear cone assembly of a jet engine.

Author Contributions: Fabian Bleier, a PhD candidate at ITS, designed, performed, and analysed the experiments, and wrote the manuscript. Corina Schwitzke, a senior scientist at ITS, contributed to the design and the analysis of the experiment, and to the manuscript. Hans-Jörg Bauer, professor and head of ITS, initialized the study and acted as a project leader.

Conflicts of Interest: The authors declare no conflict of interest.

Abbreviations

The following abbreviations are used in this manuscript:

Latin Symbols

A	Area (m^2)
d	Diameter (m)
C	Coefficient of a model (variable)
H	Structural thickness (m)
L	Characteristic length (m)
$\dot{Q}$	Heat flux (W)
T	Temperature (K)
$\dot{V}$	Volumetric flow (m^3/s)
W	Mechanical power (W)
c_p	Specific heat (J/(kg K))
e	Exponent of a model (–)
h	Heat transfer coefficient (W/m^2/K)
k	Thermal conductivity (W/(m K))
$\dot{m}$	Mass flow (kg/s)
n	Number of inlet holes (–)
p	Pressure (Pa)
$\dot{q}$	Heat flux density (W/m^2)
r	Radial coordinate (m)
s	Gap width (m)
u	Radial velocity component $u = u_r$ (m/s)
z	Axial coordinate (m)

Greek Symbols

Δ	Absolute uncertainty (variable)
γ	Incidence angle (rad)
μ	Dynamic viscosity (Pa s)
ν	Kinematic viscosity (m/s^2)
ω	Angular velocity (rad/s)
φ	Angular coordinate (rad)
ϱ	Density (kg/m^3)
σ	Normal stress (N/m^2)
θ	Cone angle (rad)

Non-dimensional Groups

Bi	Biot number $Bi = h \cdot H / k_\text{S}$

Non-dimensional Groups

C_w	Non-dim. mass flow $C_w = \dot{m} / (\mu \cdot r_{\mathrm{o}}) = \dot{V} / (v \cdot r_{\mathrm{o}})$
D	Non-dim. jet hole diameter $D = d / (2 \cdot r_{\mathrm{o}})$
Ec	Eckert number $Ec = u^2 / (c_p \cdot \Delta T)$
G	Gap ratio $G = s / r_{\mathrm{o}}$
K_1	Core rotation factor at gap inlet $K_1 = (\cos \gamma \cdot u_{\mathrm{jet}}) / (r_{\mathrm{o}} \cdot \omega)$
Nu	Nusselt number $Nu = h \cdot r_{\mathrm{o}} / k_{\mathrm{f}}$
$\overline{Nu}$	Global Nusselt number $\overline{Nu} = \int Nu \cdot \Delta T \, \mathrm{d}A / \int \Delta T \, \mathrm{d}A$
Pr	Prandtl number $Pr = \mu \cdot c_p / k$
Re	Reynolds number $Re = u \cdot r_{\mathrm{o}} / v$
X	Radius ratio $X = r_{\mathrm{i}} / r_{\mathrm{o}}$
R	Recovery factor $R = Pr^{1/3}$

Indices

1	Gap inlet property
ad	Adiabatic
c	Cooled
f	Fluid
h	Heated
i	Inner
jet	Jet
o	Outer
φ	Circumferential
S	Solid
W	Wall
L	Leakage

Abbreviations

RMSE	Root Mean Square Error

Appendix A. Finite-Element Model

The local heat flux density $\dot{q}_{\mathrm{S}}$ of the rotor surface is calculated by a two-dimensional, axisymmetric finite-element model. The boundary conditions are depicted in Figure A1a. The temperature boundary conditions are derived by spline interpolation of the measured temperatures (■). At the outer and inner rotor radius no temperature measurement was realized (——). However, a sensitivity study has shown that the boundary conditions in these regions do not affect the temperature distribution in the region of interest. Therefore, the temperatures of the adjacent measurements are used and extrapolated to these regions. The distance between the temperature measurements was chosen according to temperature distributions derived from CFD results. An additional study showed that maximum errors of 2% of the global Nusselt numbers occur when switching the interpolation scheme from spline to linear, indicating a proper distribution of the temperature measurements. The edge length of the quadratic finite elements is approximately 1 mm. Subsequently, the heat flux $\dot{Q}_{\mathrm{S}}$ between the inlet radius r_1, and the evaluation radius r^* can be calculated by numerically integrating the local heat flux density. Therefore, the rotor surface has been discretised according to Figure A1b with an edge length $\ll 1$ mm.
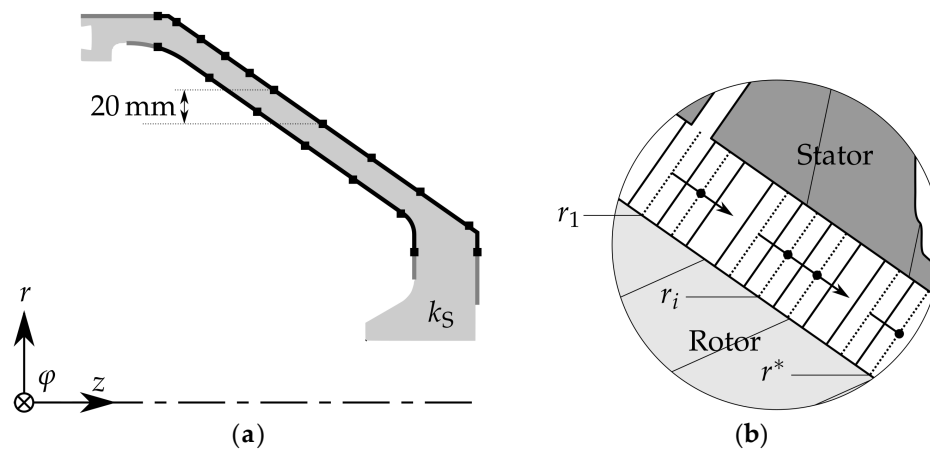
Figure A1. Boundary conditions of finite-element model and discretization of the rotor-stator system. (**a**) Finite-element model including boundary conditions: interpolated temperature and measurement point (━■━), extrapolated temperature (──). (**b**) Discretization of the rotor-stator gap to calculate the adiabatic wall temperature.

Appendix B. Adiabatic Wall Temperature

The local adiabatic wall temperature is derived using the equation [8]

$$T_{\text{W,ad}} = T_{\text{f}}(r) - \frac{u^2}{2 \cdot c_p} + R \cdot \frac{(\omega r - u)^2}{2 \cdot c_p}, \tag{A1}$$

where the recovery factor $R = Pr^{1/3}$. The local total fluid temperature $T_{\text{f}}(r)$ depends on the total inlet temperature T_{f}, the heat flux $\dot{Q}_{\text{S}}$, the transferred mechanical power W, and the mass flow rate $\dot{m}$ leading to the local adiabatic wall temperature

$$T_{\text{W,ad}} = T_{\text{f}} + \frac{\dot{Q}_{\text{S}} + W}{\dot{m} \cdot c_p} - \frac{u^2}{2 \cdot c_p} + R \cdot \frac{(\omega r - u)^2}{2 \cdot c_p}. \tag{A2}$$

The locally transferred mechanical power W can be derived from the local heat transfer by applying the modified Reynolds analogy [8]. This assumption has been proven based on CFD results, leading to an error between the CFD results and applying the Reynolds analogy to the CFD results of maximum 15%.

The local free stream velocity u yields from evaluating the pressure gradient along the rotor-stator gap. In flows with dominant circumferential velocity the relationship

$$u = \sqrt{\frac{r}{\varrho} \cdot \frac{\partial p}{\partial r}}, \tag{A3}$$

where r is the local Radius and ϱ is the fluid density, is valid. The pressure gradient $\partial p / \partial r$ is calculated from the spline interpolated stator wall pressures measured with radial distances of 50 mm. The validation of Equation (A3) for the present rotor-stator system was done by CFD calculations leading to maximum errors of 15% between CFD results and Equation (A3).

References

1. Von der Bank, R.; Donnerhack, S.; Rae, A.; Cazalens, M.; Lundbladh, A.; Dietz, M. LEMCOTEC—Improving the Core-Engine Thermal Efficiency: Paper-Nr. GT2014-25040. In Proceedings of the ASME Turbo Expo 2014: Turbine Technical Conference and Exposition, Düsseldorf, Germany, 16–20 June 2014.
2. Kervistin, R. Cooling System for a Gas Turbine Engine Compressor. U.S. Patent No. 5297386, 29 March 1994.

3.   Bleier, F.; Hufnagel, M.; Pychynski, T.; Eichler, C.; Bauer, H.J. Numerical Conjugate Heat Transfer Study of a Cooled Compressor Rear Cone: Paper-Nr. GT2014-26289. In Proceedings of the ASME Turbo Expo 2014: Turbine Technical Conference and Exposition, Düsseldorf, Germany, 16–20 June 2014.

4.   Bleier, F.; Höfler, C.; Pychynski, T.; Bauer, H.J. Design and Validation of a Test Rig for Heat Transfer Measurements on a Rotating Cone: Paper-Nr. ISABE-2015-20273. In Proceedings of the 22nd International Symposium on Air Breathing Engines, Phoenix, AZ, USA, 25–30 October 2015.

5.   Fénot, M.; Bertin, Y.; Dorignac, E.; Lalizel, G. A review of heat transfer between concentric rotating cylinders with or without axial flow. *Int. J. Therm. Sci.* **2011**, *50*, 1138–1155. [CrossRef]

6.   Harmand, S.; Pellé, J.; Poncet, S.; Shevchuk, I.V. Review of fluid flow and convective heat transfer within rotating disk cavities with impinging jet. *Int. J. Therm. Sci.* **2013**, *67*, 1–30. [CrossRef]

7.   Owen, J.M.; Rogers, R.H. *Flow and Heat Transfer in Rotating-Disc Systems: Rotating Cavities*; Research Studies Press: Taunton, UK; John Wiley & Sons: New York, NY, USA, 1995; Volume 2.

8.   Owen, J.M.; Rogers, R.H. *Flow and Heat Transfer in rotating-Disc Systems: Rotor-Stator Systems*; Research Studies Press: Taunton, UK; John Wiley & Sons: New York, NY, USA, 1989; Volume 1.

9.   Alexiou, A.; Hills, N.J.; Long, C.A. Heat Transfer in High-Pressure Compressor Gas Turbine Internal Air Systems: A Rotating Disc-Cone Cavity with Axial Throughflow. *Exp. Heat Transf.* **2000**, *13*, 299–328. [CrossRef]

10. Wimmer, M.; Zierep, J. Transition from Taylor vortices to cross-flow instabilities. *Acta Mech.* **2000**, *140*, 17–30. [CrossRef]

11. Long, C.A.; Turner, A.B.; Kais, G.; Tham, K.M.; Verdicchio, J.A. Measurement and CFD Prediction of the Flow within an HP Compressor Drive Cone. *J. Turbomach.* **2003**, *125*, 165–172. [CrossRef]

12. Dorfman, L.A. *Hydrodynamic Resistance and the Heat Loss of Rotating Solids*; Oliver & Boyd: Edinburgh, Scotland, UK, 1963.

13. Daily, J.W.; Nece, R.E. Chamber Dimension Effects on Induced Flow and Frictional Resistance of Enclosed Rotating Disks. *J. Basic Eng.* **1960**, *82*, 217–230. [CrossRef]

14. Pellé, J.; Harmand, S. Heat transfer measurements in an opened rotor-stator system air-gap. *Exp. Therm. Fluid Sci.* **2007**, *31*, 165–180. [CrossRef]

15. Mitchell, J.W.; Metzger, D.E. Heat Transfer From a Shrouded Rotating Disk to a Single Fluid Stream. *J. Heat Transf.* **1965**, *87*, 485. [CrossRef]

16. Djaoui, M.; Dyment, A.; Debuchy, R. Heat transfer in a rotor-stator system with a radial inflow. *Eur. J. Mecha.-B/Fluids* **2001**, *20*, 371–398. [CrossRef]

17. Tang, H.; Shardlow, T.; Michael Owen, J. Use of Fin Equation to Calculate Nusselt Numbers for Rotating Disks. *J. Turbomach.* **2015**, *137*, 121003. [CrossRef]

18. Geis, T. Strömung und Reibungsinduzierte Leistungs- und Wirkungsgradverluste in Komplexen Rotor-Stator Zwischenräumen. Ph.D. Thesis, Department of Mechanical Engineering, University of Karlsruhe, 2002.

19. Seber, G.A.F.; Wild, C.J. *Nonlinear Regression*; John Wiley & Sons, Inc.: Hoboken, NJ, USA, 1989.